Supplement of Atmos. Chem. Phys., 22, 2029–2047, 2022
https://doi.org/10.5194/acp-22-2029-2022-supplement

Atmospheric Chemistry and Physics
Open Access
EGU

Supplement of

Bimodal distribution of size-resolved particle effective density: results from a short campaign in a rural environment over the North China Plain

Yaqing Zhou et al.

Correspondence to: Nan Ma (nan.ma@jnu.edu.cn) and Qiaoqiao Wang (q.wang2@outlook.com)

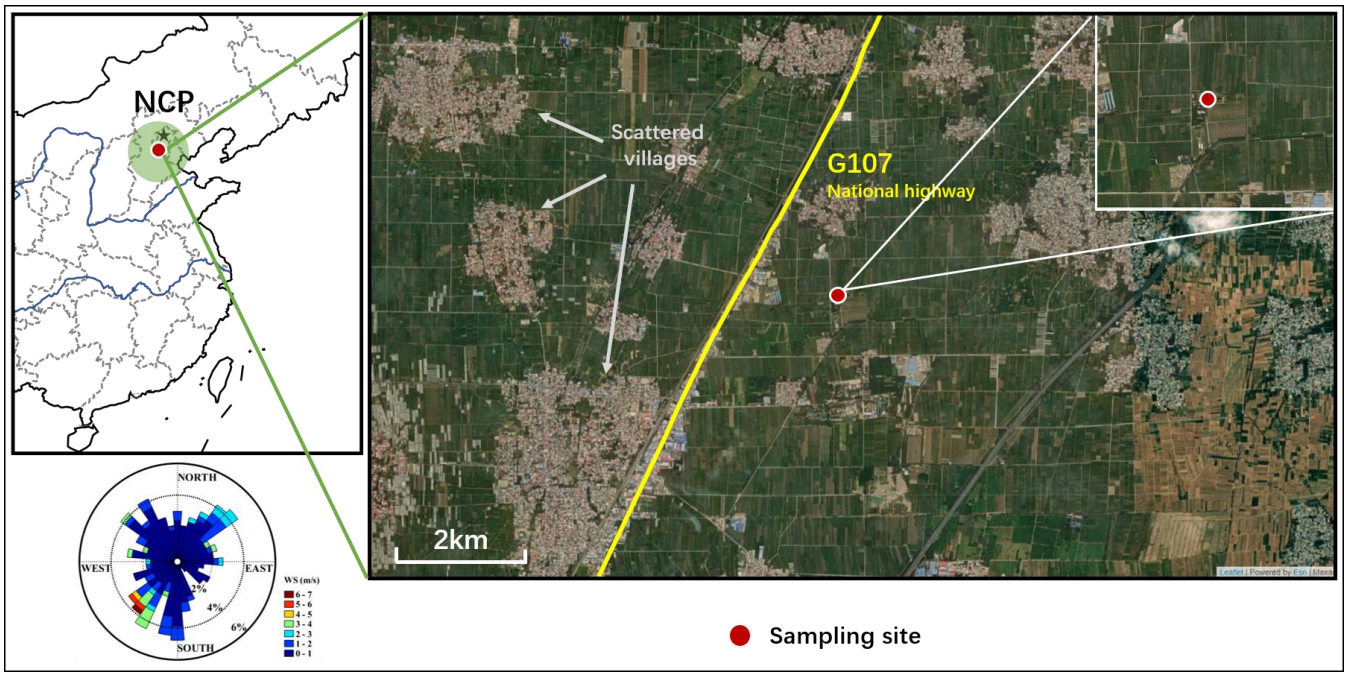

Figure S1. Location of the sampling site (marked in red circle) and statistic of wind frequency (the left-bottom of the figure). Satellite view from © ESRI.

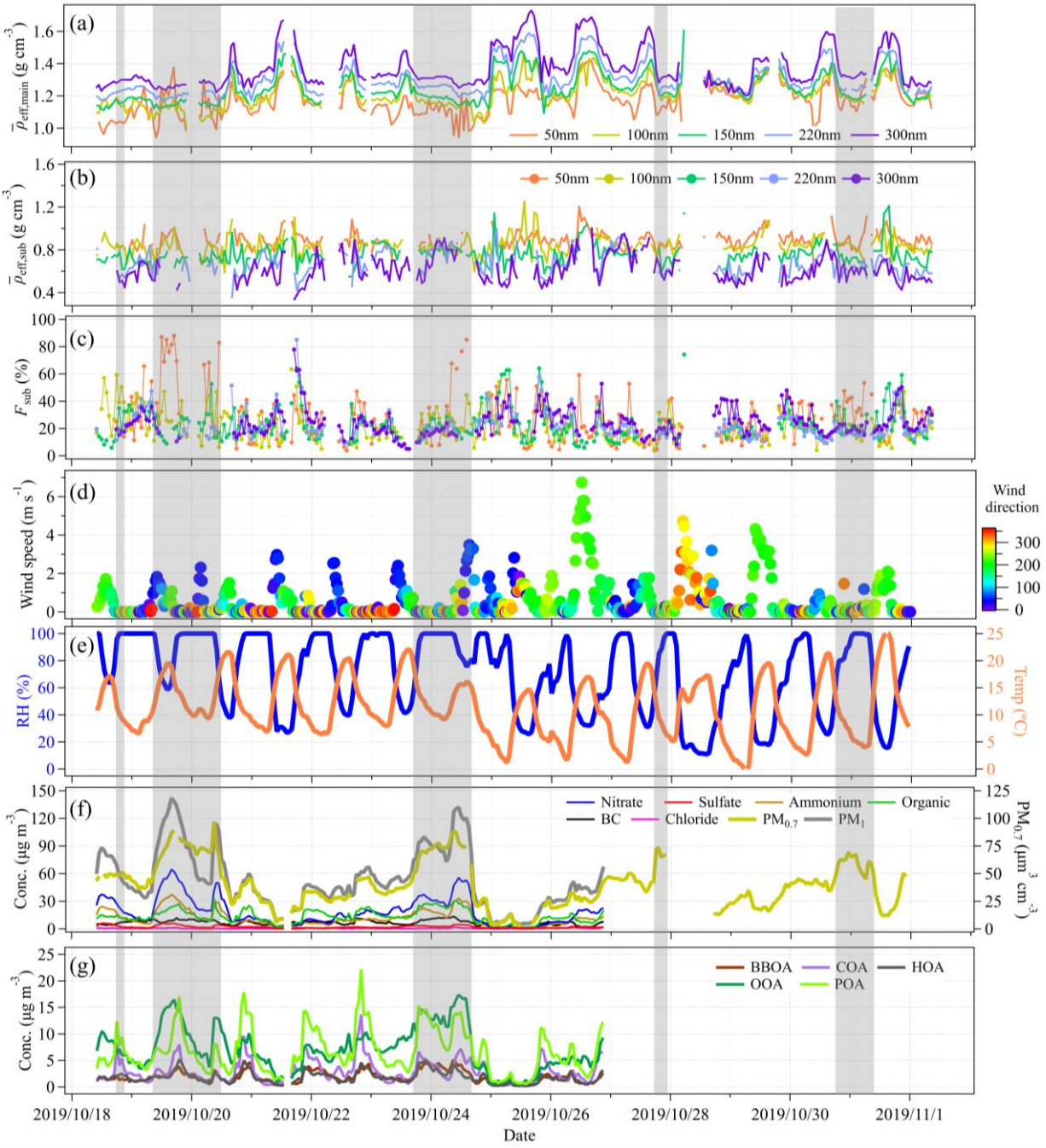

Figure S2. Timeseries of (a) geometric mean of the main density mode ($\bar{\rho}_{\mathrm{eff,main}}$), (b) geometric mean of the sub-density mode ($\bar{\rho}_{\mathrm{eff,sub}}$), (c) number fraction of the sub-density mode (F_{sub}), (d) wind speed and wind direction, (e) relative humidity and temperature, (f) mass concentration of PM_1 chemical composition and (g) mass concentration of OA sources. The grey shaded areas represent the more polluted periods ($PM_{0.7}$ > 50 μm^3 cm^{-3}).

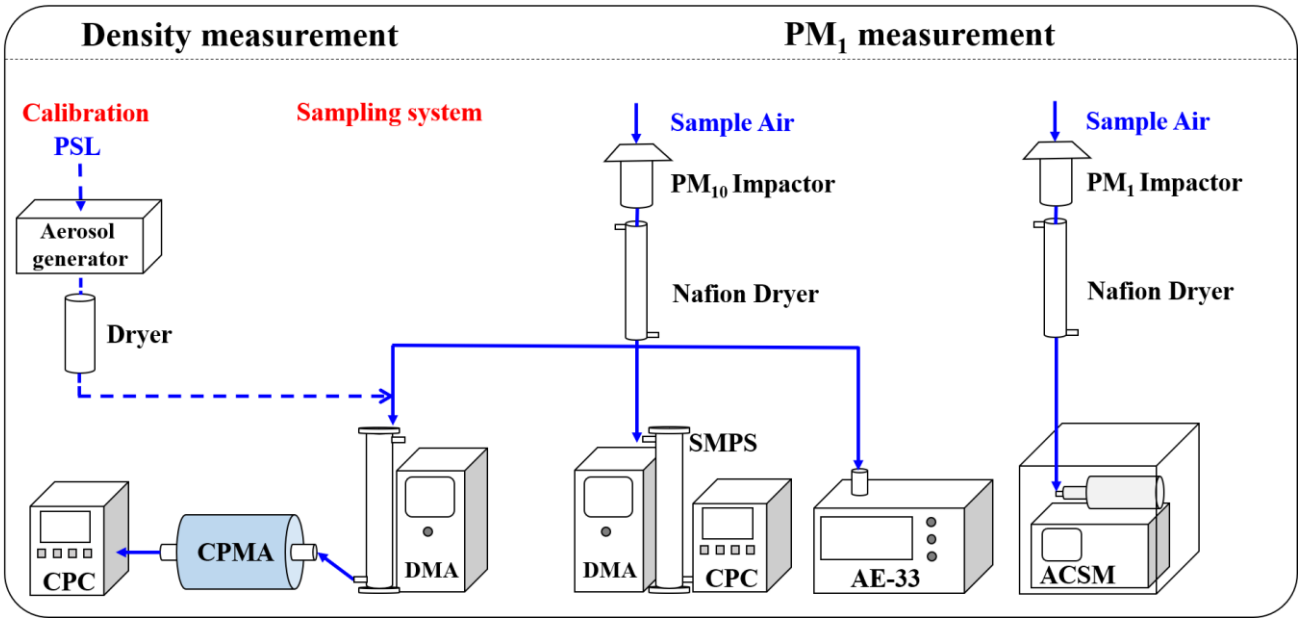

Figure S3. Schematic diagram for particle effective density and PM_1 measurement.

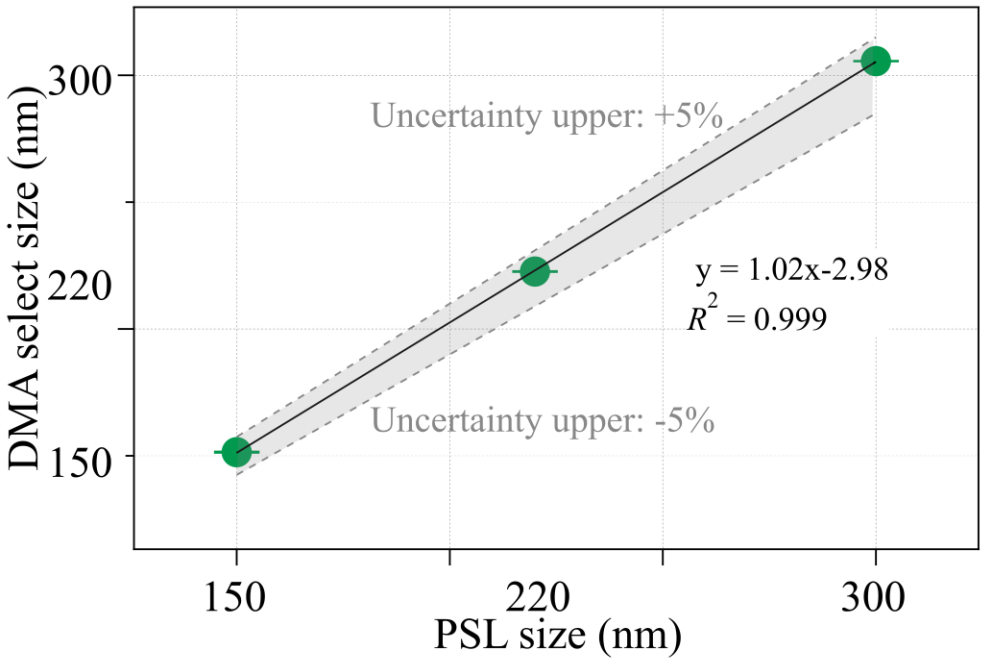

Figure S4. Uncertainty of DMA size selection.

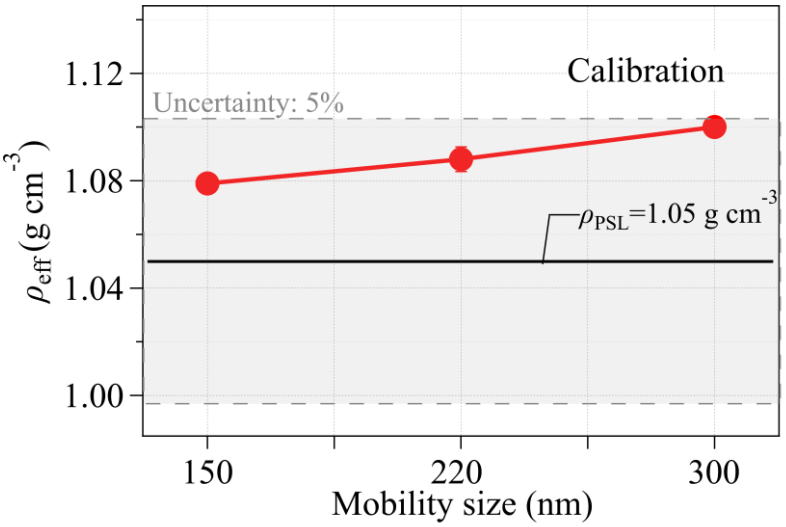

Figure S5. Calibration results for DMA-CPMA-CPC system.

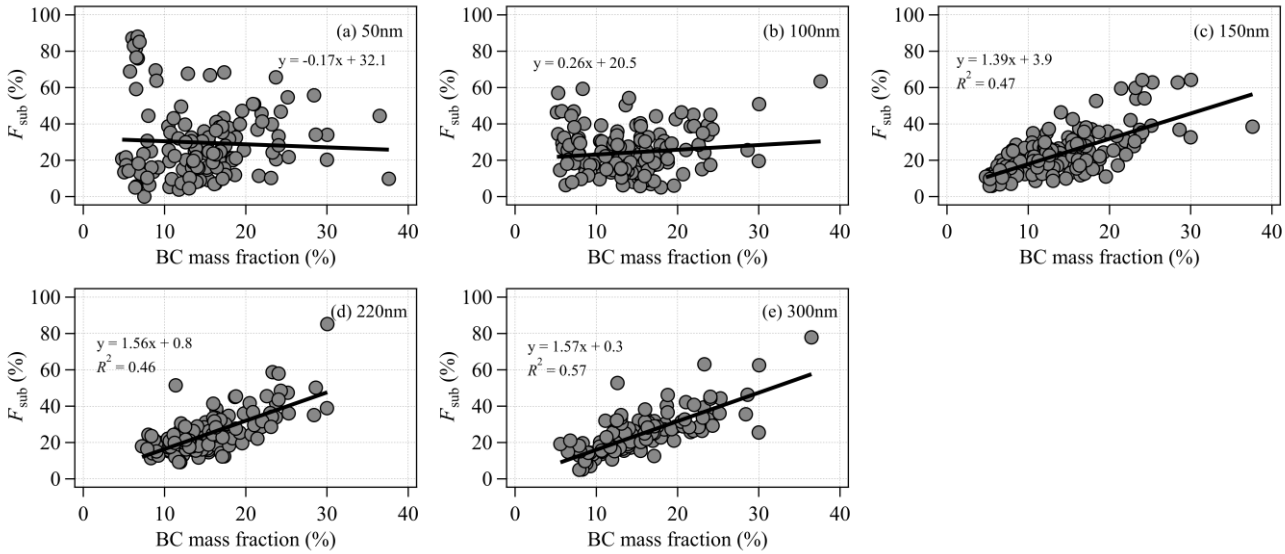

Figure S6. Correlation between BC mass fraction and the number fraction of the sub-density mode (F_{sub}) for (a) 50 nm, (b) 100 nm, (c) 150 nm, (d) 220 nm, and (e) 300 nm particles.

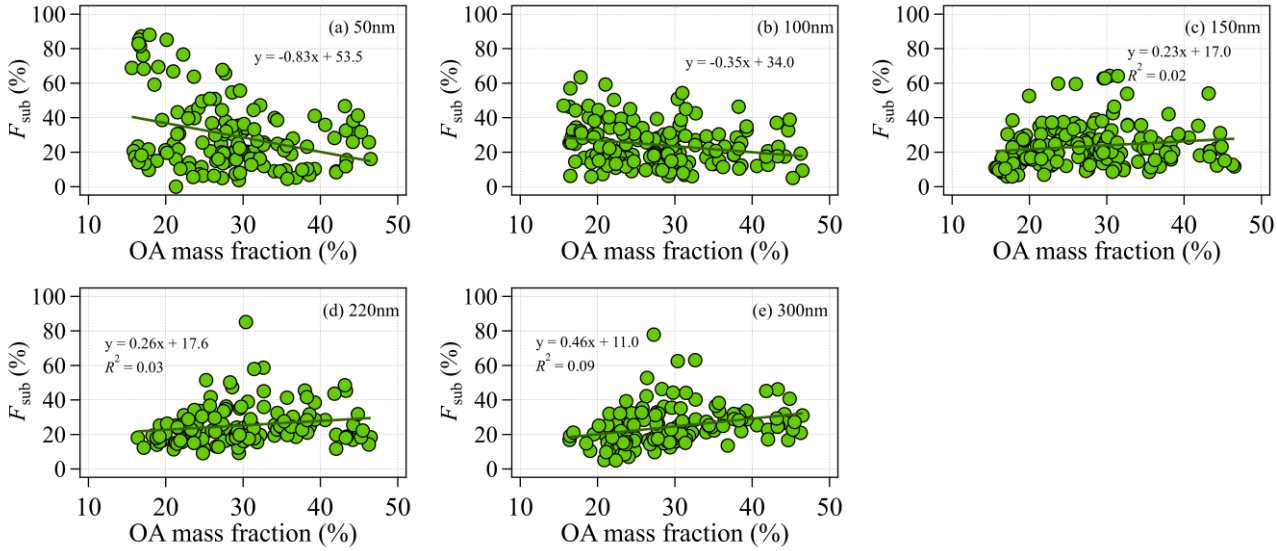

Figure S7. Correlation between OA mass fraction and the number fraction of the sub-density mode (F_{sub}) for (a) 50 nm, (b) 100 nm, (c) 150 nm, (d) 220 nm, and (e) 300 nm particles.

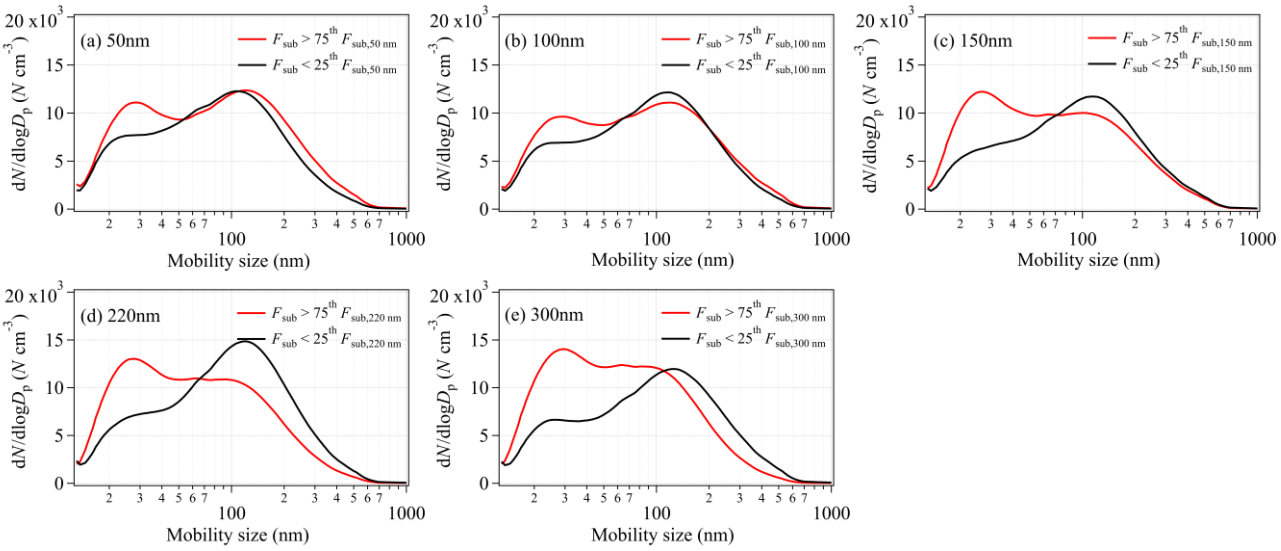

Figure S8. Particle number size distribution with high F_{sub} (F_{sub} > 75th F_{sub}) and low F_{sub} (F_{sub} < 25th F_{sub}) values for (a) 50 nm, (b) 100 nm, (c) 150 nm, (d) 220 nm, and (e) 300 nm particles.

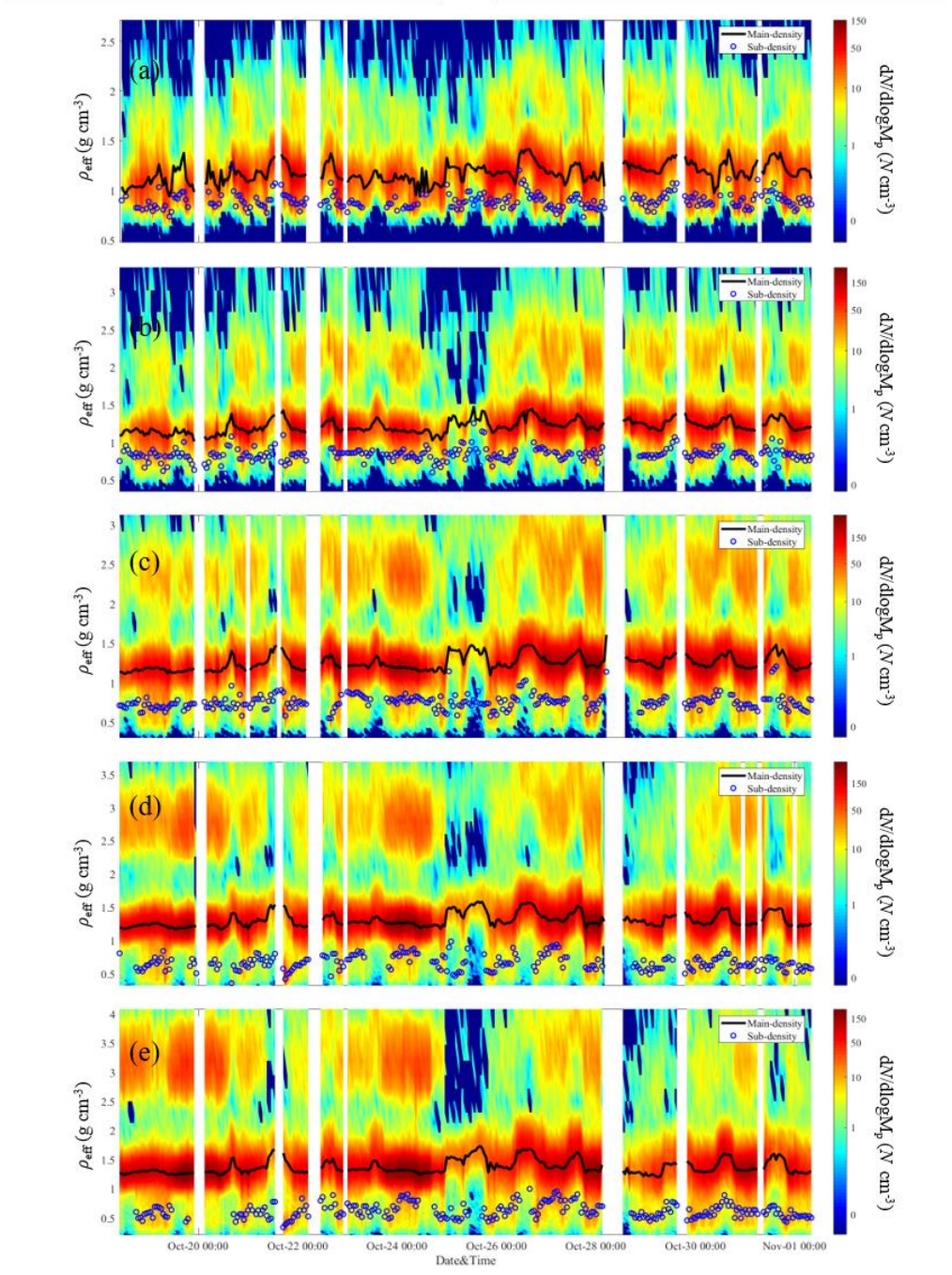

Figure S9. Particle effective density (ρ_{eff}) distribution for (a) 50 nm, (b) 100 nm, (c) 150 nm, (d) 220 nm, and (e) 300 nm particles during the entire sampling period. The black lines and blue circles represent the geometric mean for the main density mode ($\bar{\rho}_{eff,main}$) and the sub-density mode ($\bar{\rho}_{eff,sub}$) respectively.

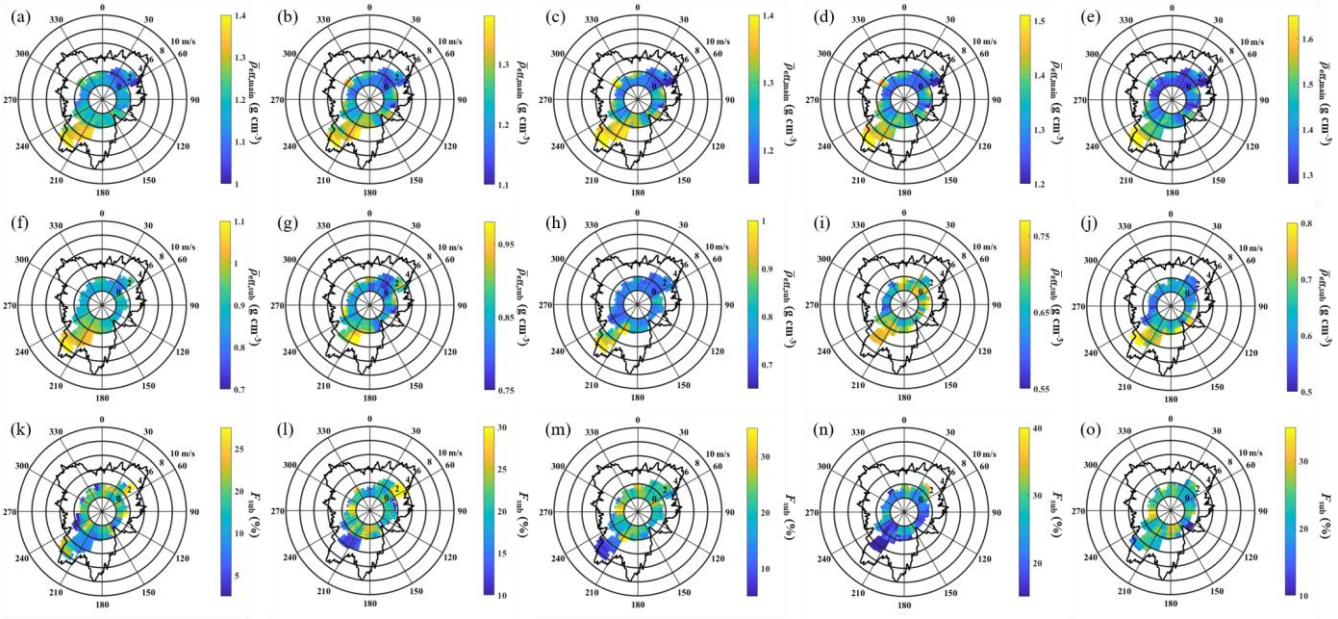

Figure S10. Wind rose analysis of (a)-(e): geometric mean of the main density mode ($\bar{\rho}_{\mathrm{eff,main}}$), (f)-(j): geometric mean of the sub-density mode ($\bar{\rho}_{\mathrm{eff,sub}}$), (k)-(o): number fraction of the sub-density mode (F_{sub}) for 50, 100, 150, 220 and 300 nm particles. Black bold lines represent wind frequency during the entire sampling period.

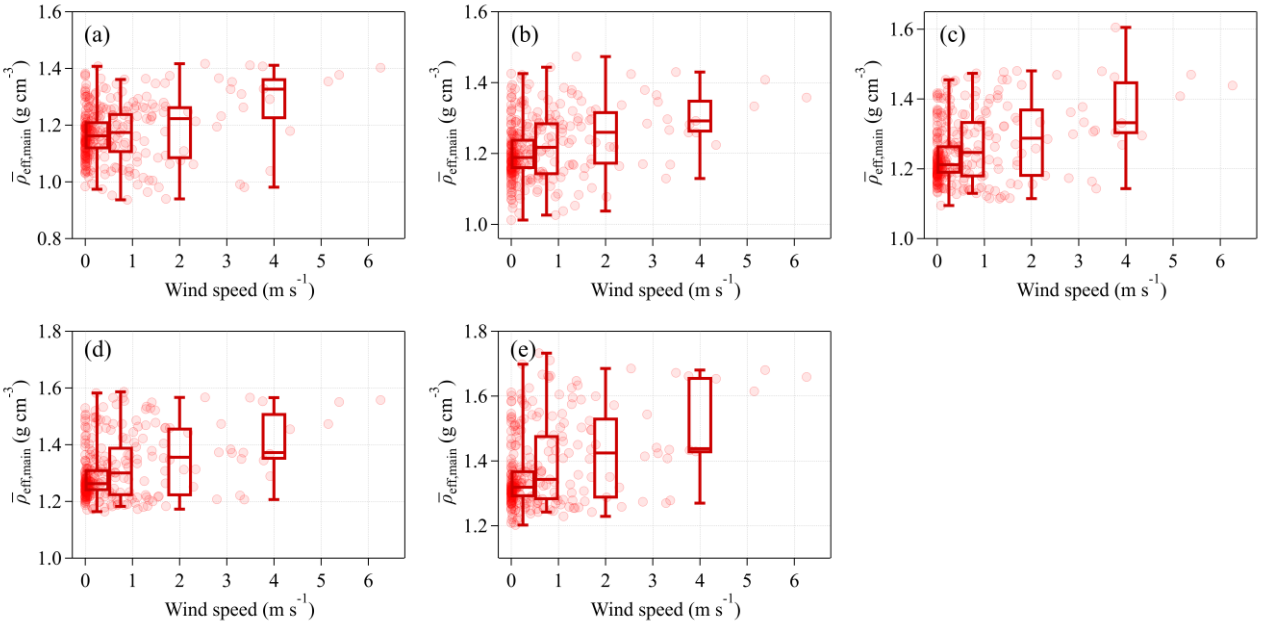

Figure S11. Box plots of geometric mean of the main density mode ($\bar{\rho}_{\mathrm{eff,main}}$) versus wind speed for (a) 50 nm, (b) 100 nm, (c) 150 nm, (d) 220 nm, and (e) 300 nm particles.

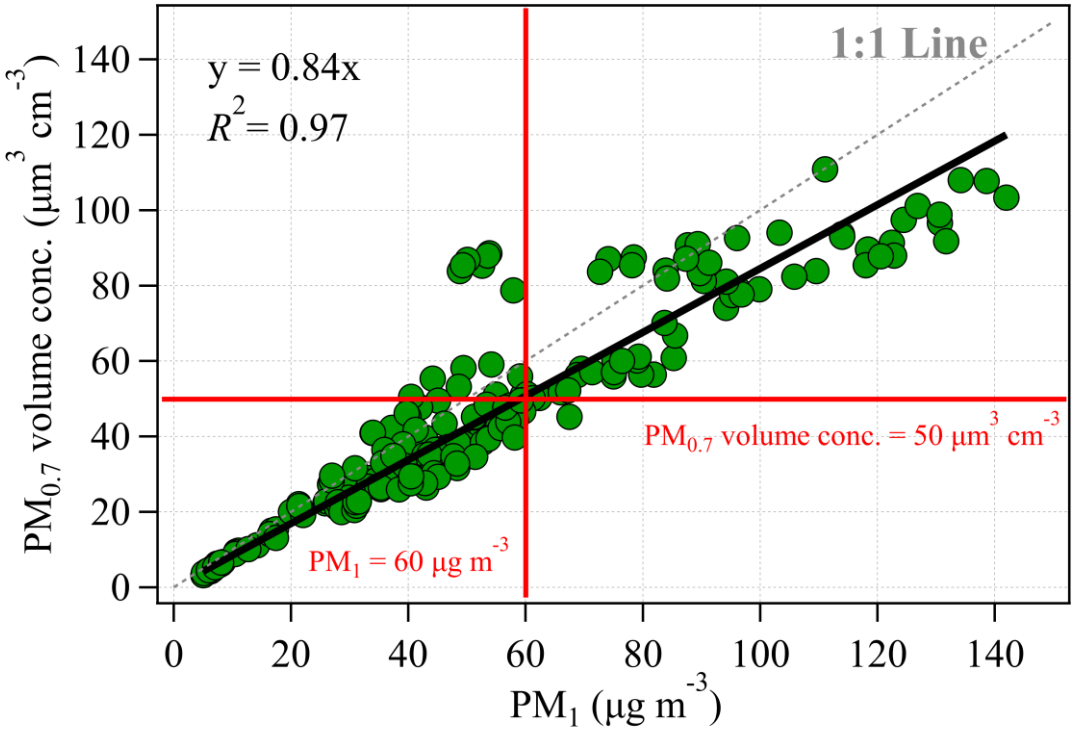

Figure S12. Comparison of $PM_{0.7}$ volume concentration and PM_1 mass concentration.

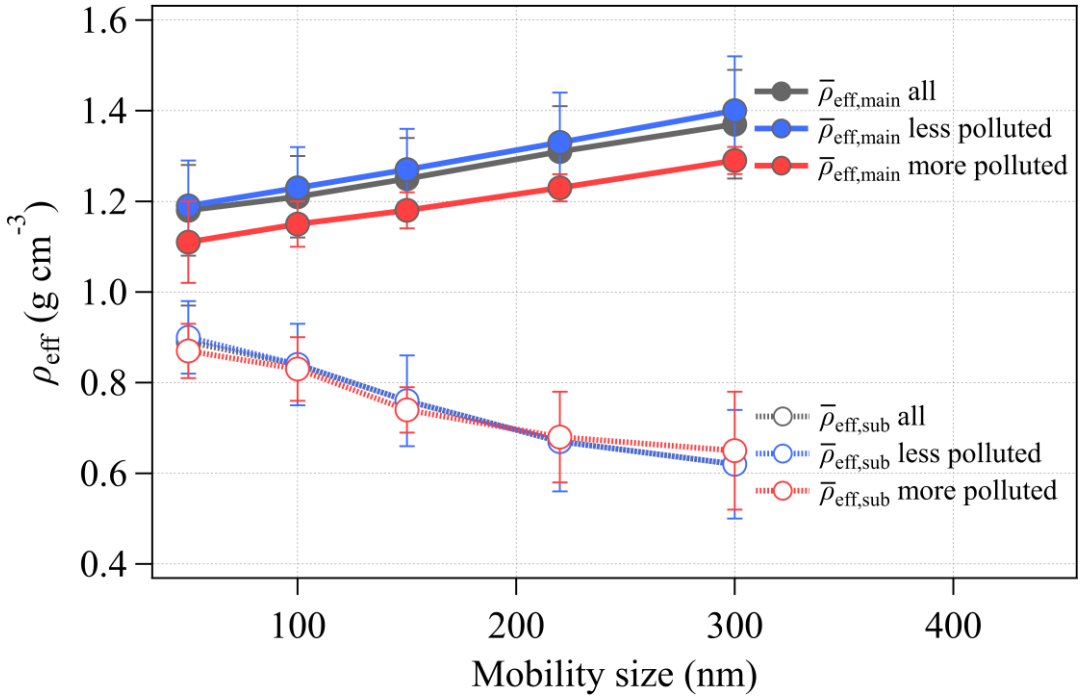

Figure S13. Trend lines of effective density (ρ_{eff}) against mobility size for the entire sampling period, the more and the less polluted conditions.

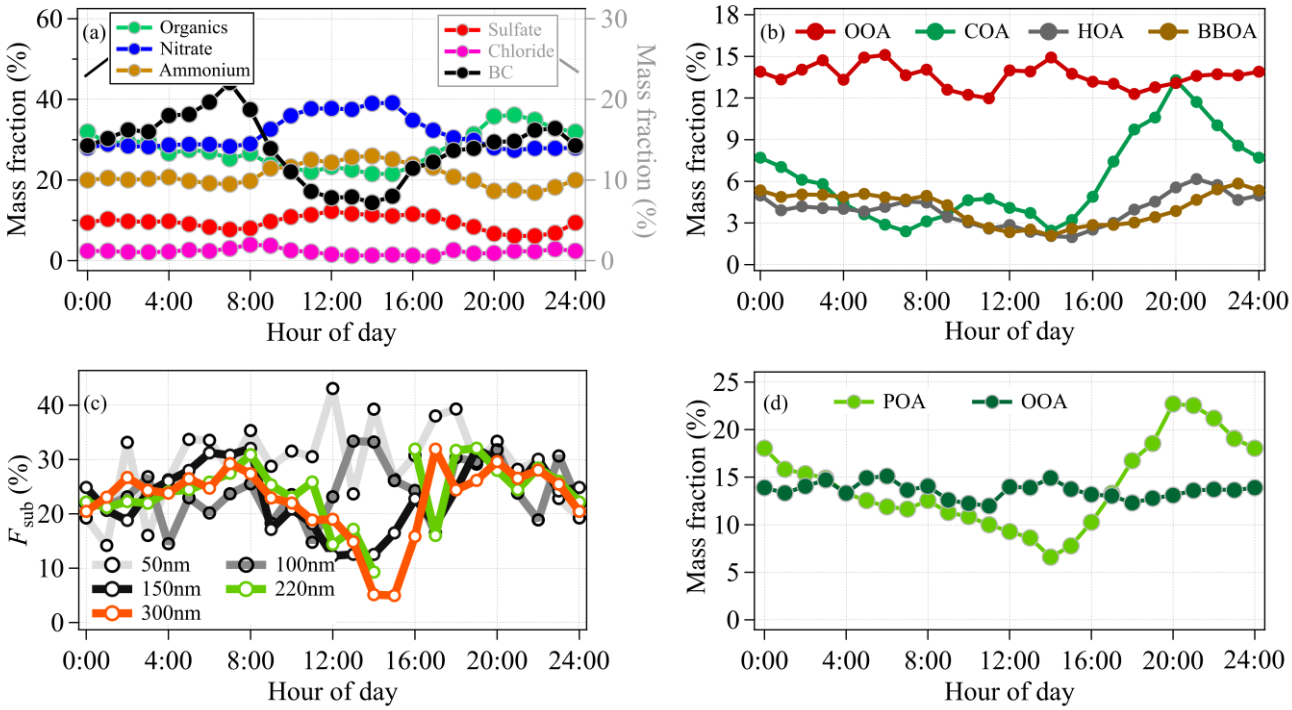

Figure S14. Diurnal cycle of (a) organics, nitrate, ammonium, sulfate, chloride and BC mass fractions, (b) OOA, COA, HOA and BBOA mass fractions, (c) number fraction of the sub-density mode (F_{sub}), (d) primary (POA) and secondary organic aerosols (SOA) mass fractions.

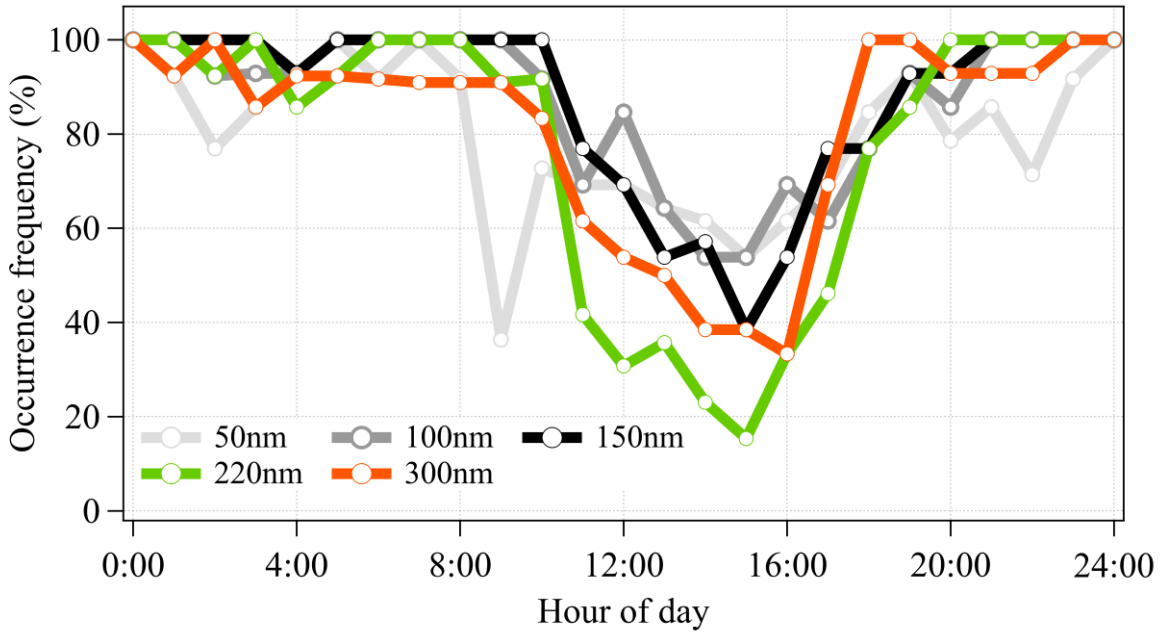

Figure S15. Diurnal cycle of the occurrence frequency of the sub-density mode at five mobility sizes.

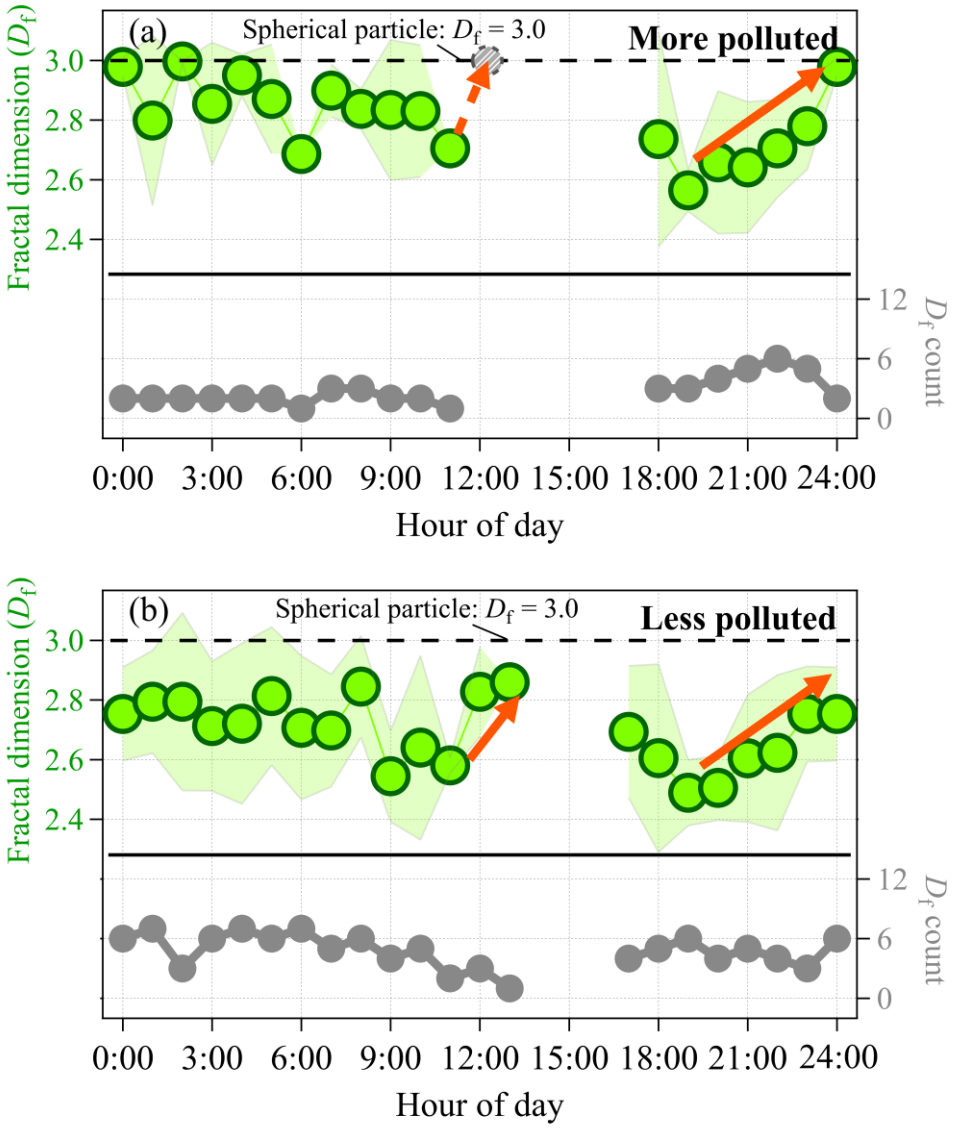

Figure S16. Diurnal cycle of fractal dimension (D_f) of the sub-density mode particles and D_f count under (a) the more and (b) the less polluted conditions. The dotted line is D_f with the value of 3.0, indicating particle with a spherical morphology. The orange arrows represent D_f with increasing trend. The grey dotted circle in the top figure represents the assumption of D_f = 3.0 at 13:00.

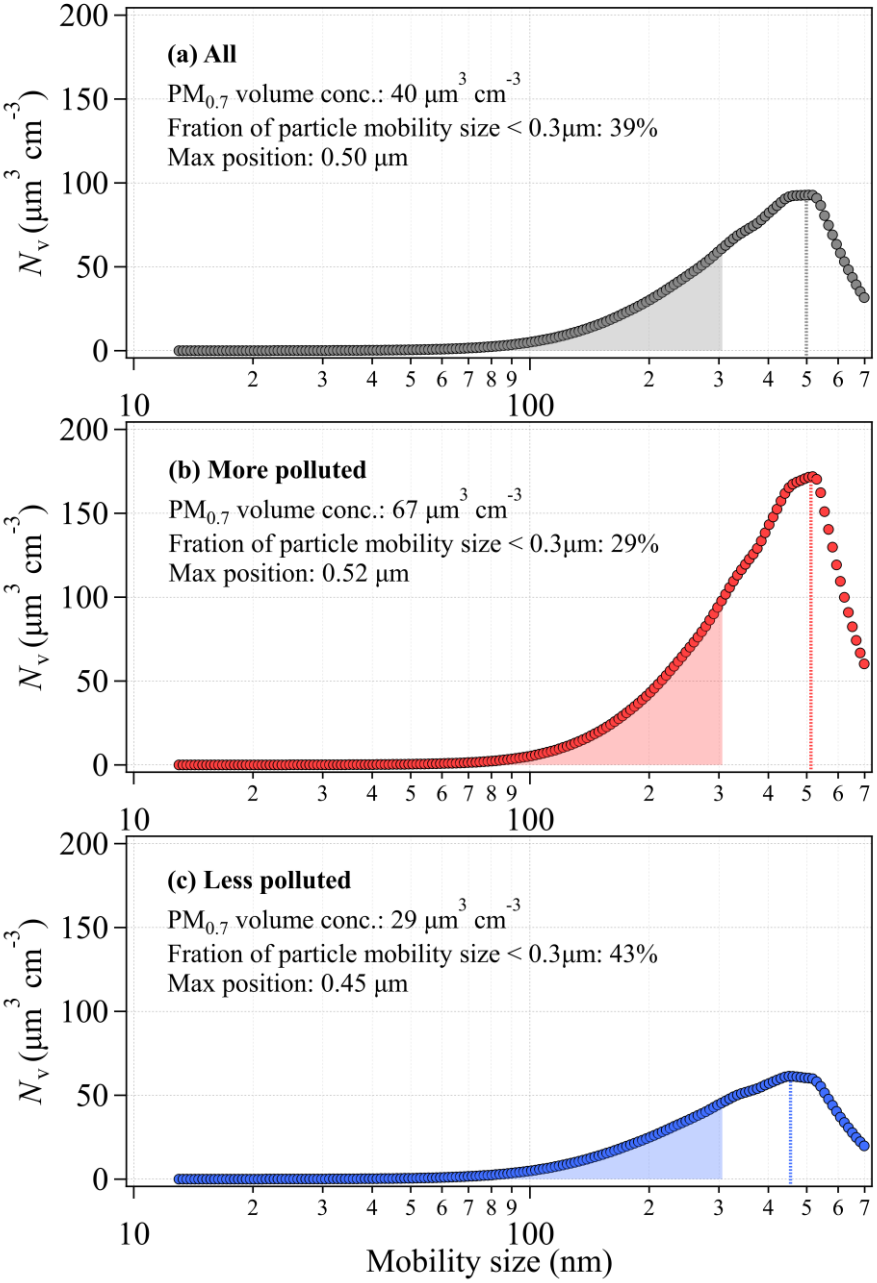

Figure S17. Volume distribution of $PM_{0.7}$ during (a) the entire sampling period, (b) the more polluted and (c) the less polluted conditions. The shaded areas are volume distributions for particles below 300 nm, and vertical dotted lines are the peak positions of $PM_{0.7}$ volume size distribution.

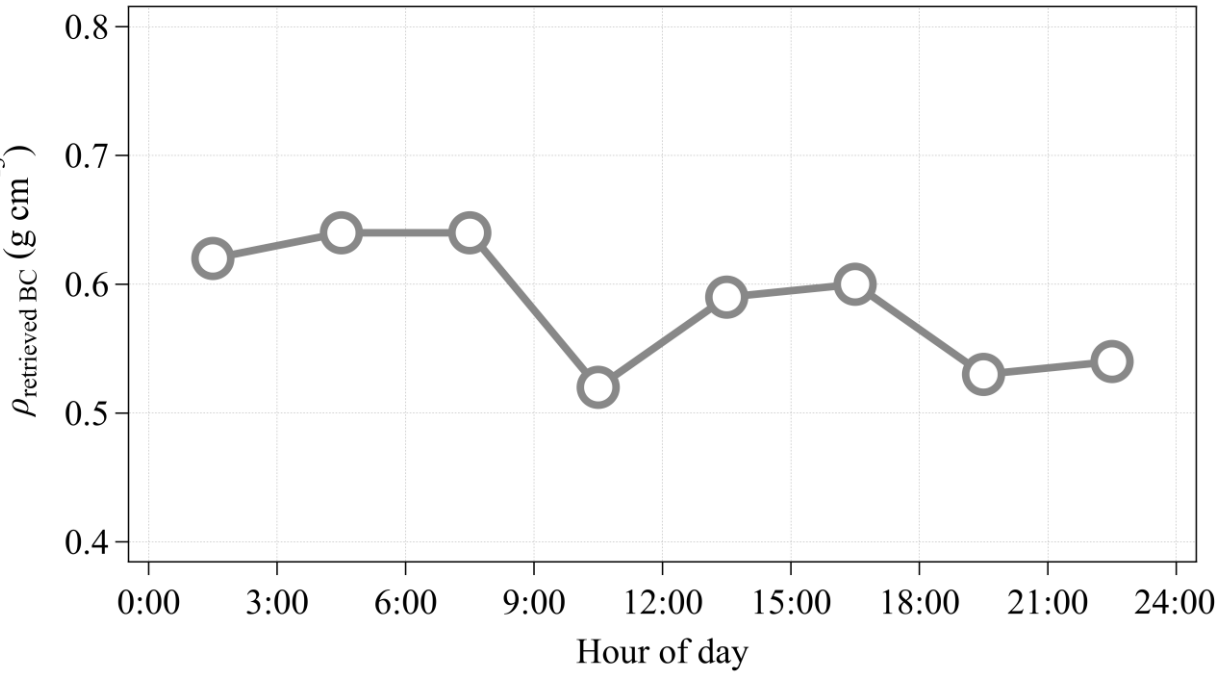

Figure S18. Diurnal variation of retrieved BC effective density.

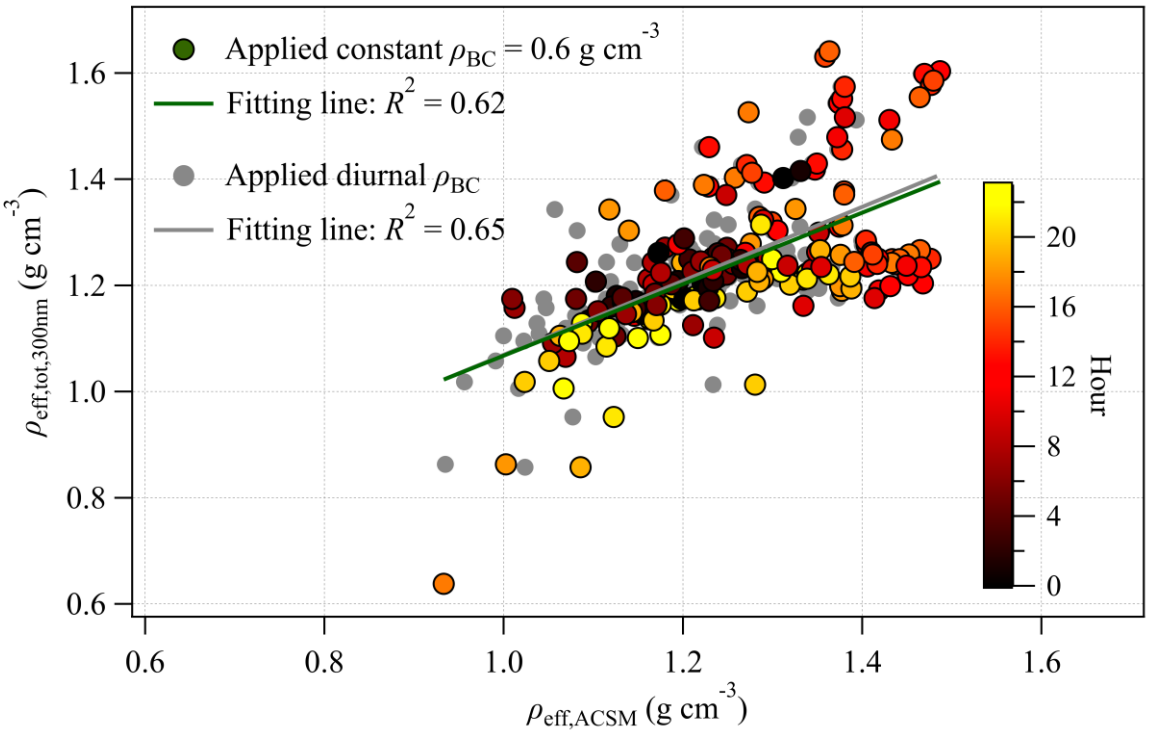

Figure S19. Comparison of the average effective density of particles at 300 nm observed by DMA-CPMA-CPC ($\bar{\rho}_{eff,tot,300nm}$) and ACSM-derived bulk effective density ($\rho_{eff,ACSM}$) by applied a constant ρ_{BC} or diurnal varied ρ_{BC}.

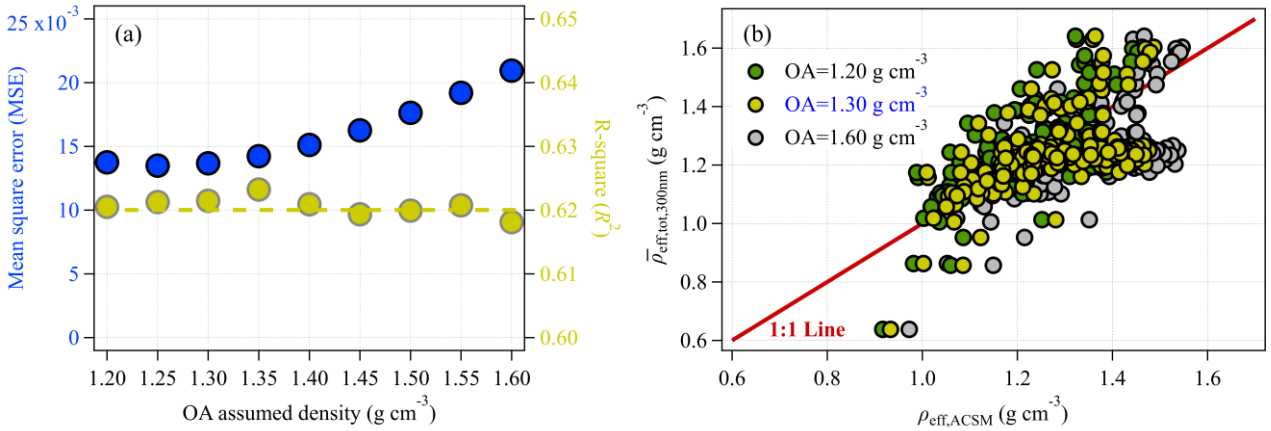

Figure S20. (a) Mean square error (MSE) and R-square (R^2) results from OA density sensitivity test. (b) Comparison of the average effective density of particles at 300 nm observed by DMA-CPMA-CPC ($\bar{\rho}_{\mathrm{eff,tot,300nm}}$) and ACSM-derived bulk effective density ($\rho_{\mathrm{eff,ACSM}}$). The colored dots in the right figure represent $\rho_{\mathrm{eff,ACSM}}$ based on different OA density assumption. Red line in the right figure is the line with slope of 1.

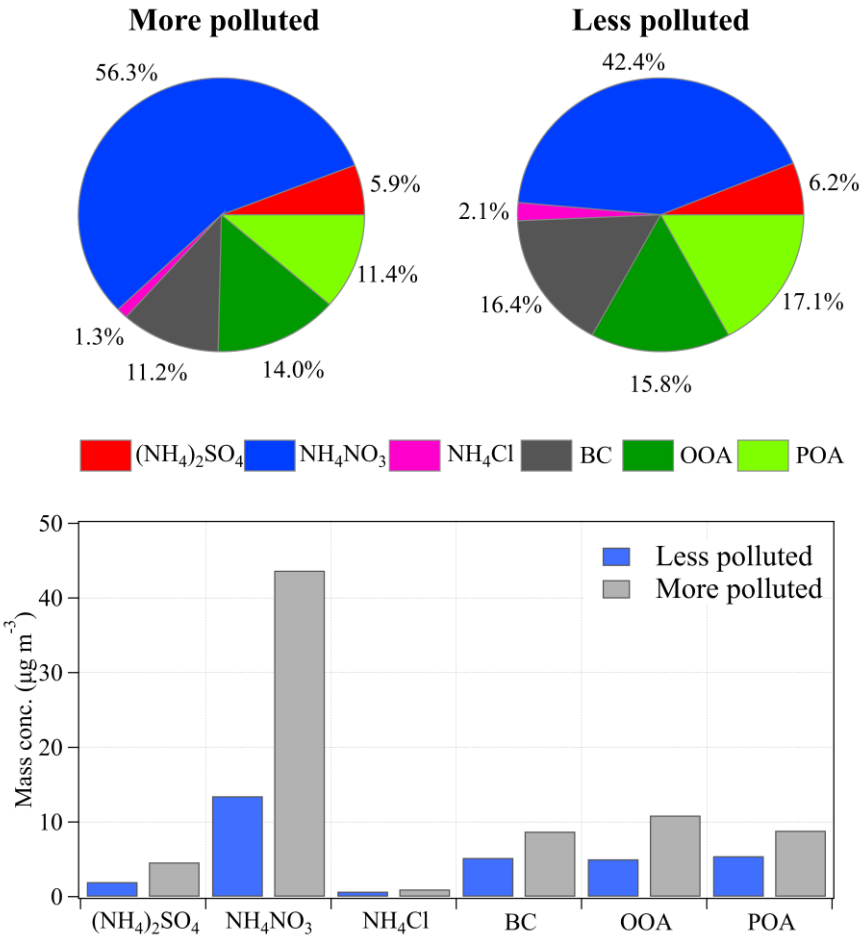

Figure S21. The mass fraction (top of the figure) and mass concentration (bottom of the figure) of PM_1 chemical components under the more and the less polluted conditions.

Table S1. Doubly charge estimation for five mobility size

size(nm)	$\bar{\rho}_{\text{eff,main}}$(g cm^{-3})	size$_{\text{double}}$[a](nm)	ρ_{double}[b](g cm^{-3})	k_{double}[c]
50	1.18	73	1.16	1.59
100	1.21	151	1.23	1.78
150	1.25	235	1.30	2.05
220	1.31	360	1.42	2.39
300	1.37	510	1.55	2.80

[a] mobility size of doubly charged particles after penetrate DMA based on Boltzmann distribution
[b] effective density at each size$_{\text{double}}$ retrieved from linear fit equation of $\bar{\rho}_{\text{eff,main}}$
[c] the ratio of geometric mean of doubly charged mass to single charge mass in CPMA mass distribution